Applying Deep Learning to NASA MODIS Data to Create a Community Record of Marine Low Cloud Mesoscale Morphology

Tianle Yuan[1,2], Hua Song[3], Robert Wood[4], Johannes Mohrmann[4], Kerry Meyer[1], Lazaros Oreopoulos[1], Steven Platnick[1]

[1]Earth Science Directorate, NASA Goddard Space Flight Center

[2]Joint Center for Earth Systems Technology, University of Maryland, Baltimore County

[3]Science Systems and Applications, Inc.

[4]Department of Atmospheric Sciences, University of Washington

Correspondence: tianle.yuan@nasa.gov

Abstract:

Marine low clouds display rich mesoscale morphological types, distinct spatial patterns of cloud fields. Being able to differentiate low cloud morphology offers a tool for the research community to go one step beyond bulk cloud statistics such as cloud fraction and advance the understanding of low clouds. Here we report the progress of our project that aims to create an observational record of low cloud mesoscale morphology at a near-global (60S-60N) scale. First, a training set is created by our team members manually labeling thousands of mesoscale (128x128) MODIS scenes into six different categories: stratus, closed cellular convection, disorganized convection, open cellular convection, clustered cumulus convection, and suppressed cumulus convection. Then we train a deep convolutional neural network model using this training set to classify individual MODIS scenes at 128x128 resolution, and test it on a test set. The trained model achieves a cross-type average precision of about 93%. We apply the trained model to 16 years of data over the Southeast Pacific. The resulting climatological distribution of low cloud morphology types shows both expected and unexpected features and suggests promising potential for low cloud studies as a data product.

1. Introduction

Marine low clouds are important for the mass, heat, and momentum transport in the planetary boundary layer (PBL) and between the PBL and free troposphere, the radiative energy balance of the climate, and the magnitude of feedback strength under climate change. Observations of marine low clouds are indispensable for advancing our understanding of these clouds for deriving new theories and insights and for model validation and constraining. Modern satellite observations have the advantage of providing global and long-term coverage. Current satellite products offer detailed pixel-level retrievals of cloud properties such as cloud optical depth, cloud droplet effective radius, and cloud phase. Most cloud classification schemes are based on either single pixel measurements or joint-histograms of two cloud properties.

41 However, marine low clouds are known to have various mesoscale morphology types since first
42 satellite observations of clouds became available (Agee and Dowell, 1974). These mesoscale
43 morphology types are created by the characteristic patterns into which clouds are organized
44 (Figure 1). Cloud mesoscale morphology types are not only phenological classifications of
45 satellite images, but also manifestation of complex mixture of underlying physical processes
46 (Atkinson and Zhang, 1996; Stevens et al., 2005; Wang and Feingold, 2009; Wood, 2012; Wood
47 and Hartmann, 2006). These physical processes are critical for fundamental understanding and
48 better modeling of marine low clouds because of their impact on mass, heat, and momentum
49 transport, on radiative energy balance, and their feedbacks to climate change. Wood and
50 Hartmann (2006) trained a two-layer neural network on probability distribution functions and
51 2-d power spectra of liquid water path to classify cloud morphology into four categories for
52 256x256 scenes. The method has been successfully used to analyze morphology types and
53 associated cloud properties (McCoy et al., 2017; Muhlbauer et al., 2014).
54
55 Here we introduce a NASA funded project to classify marine low cloud observations into six
56 different mesoscale morphology types based directly on full images without engineering
57 features. The goal is to produce a community data record that spans about two decades at
58 near-global scales that will enable the research community to go beyond bulk cloud statistics
59 and will advance our understanding of low-level mesoscale convective clouds through
60 exploiting the rich spatial information content of observations. Section 2 describes the data and
61 methodology; section 3 introduces preliminary results and section 4 gives discussions of future
62 plans and outlook of the data product; section 5 concludes.
63
64 **2. Data and methods**
65
66 a. Data source
67 The primary observational data for this study are from the MODerate resolution Imaging
68 Spectrometer (MODIS) onboard the Aqua satellite. We use reflectance from channels 1
69 (0.65μm) , 3 (0.47μm), and 4 (0.55μm) and cloud optical depth, cloud droplet effective radius,
70 cloud mask, and cloud top height from the MODIS cloud product (Platnick et al., 2017) in
71 building up the training set. The spatial resolution of these parameters is 1km at nadir. The
72 cloud optical depth and effective radius retrievals are combined to produce cloud liquid water
73 path (Platnick et al., 2017). Reflectance from channel 4 is used for deep neural network model
74 training and inference, while the other MODIS observations and products are used for data
75 quality control, filtering, and contextual information, as explained below.
76
77 We first break MODIS images into 128x128 pixels scenes and filter out scenes that contain
78 significant fraction of high clouds (no more than 10%), defined as pixels with cloud top height
79 above 6km, or whose low cloud fraction is lower than 5%. We also exclude scenes whose
80 viewing zenith angle is greater than 45 degrees. Scenes with more than 10% land coverage are
81 also excluded. The resulting scenes are treated as dominated by marine low clouds.
82
83 For training purpose, we create auxiliary images that contain the broad context of the scene of
84 interest and distributions of the liquid water path and cloud top height for the scene (Figure 2).

85 The scene image together with the auxiliary images are presented to a panel of human experts
86 on the Zooniverse platform (www.zooniverse.org) for manual labeling. We intend to use the
87 same platform in the future to crowdsource the labeling task.
88
89 Spatiotemporally collocated Modern-Era Retrospective analysis for Research and Applications,
90 version 2 (MERRA-2) (Gelaro et al., 2017) data is used to provide meteorological variables for
91 each scene.
92
93 b. Morphology types
94 Marine low cloud mesoscale morphology patterns are extremely diverse. In order to keep the
95 task manageable, we settle on six representative types. They are stratus, closed cellular
96 convection, disorganized cellular convection, open cellular convection, clustered cumulus, and
97 suppressed cumulus (Figure 3). These types are by no means exhaustive given the diversity of
98 observable patterns. However, these six types are the most common and largely representative
99 of the data when we inspect a large collection of scenes. In the current version, each low cloud
100 scene will be assigned one of these six types. We also believe that these types have distinct
101 underlying physical processes. Stratus is mostly created by relatively uniform radiative cooling
102 or driven by synoptic weather systems such as fronts while closed cellular convection is driven
103 by radiative cooling and organized into distinctive honeycomb mesoscale patterns.
104 Disorganized cellular convection is characterized by a combination of elements of convection
105 and large portion of stratiform clouds that tend to have large droplet sizes and small cloud
106 optical depths, creating their characteristic appearance. Their cellular sizes are typically larger,
107 on the order of 100km, compared to closed cellular convection, on the order of 10km. Open
108 cellular convection is characterized by cells that are clear in the center and exhibit vigorous
109 shallow convection around it. These convective clouds are often precipitating based on satellite
110 and ship-based observations, which is a likely driving force that creates and maintains this
111 mesoscale morphology type (Wang and Feingold, 2009). Clustered cumulus convection is made
112 up of shallow, vigorous convective elements that aggregate together, accompanied by
113 scattered shallower and optically thinner cumulus clouds nearby. The suppressed cumulus type
114 is dominated by individual, scattered cumulus clouds that can sometimes have patterns like
115 lines and branches.
116
117 c. Method
118 To illustrate the difficulty of classifying morphology types using one-point statistics such as
119 histograms, we show the mean probability density functions (PDFs) of cloud optical depth and
120 droplet effective radius for each type in Figure 4. We randomly select 1000 scenes for each
121 cloud type from 2006 data in the Southeast Pacific region. The significant overlap between PDFs
122 of different types makes it quite hard to classify the scenes based on these PDFs. On the other
123 hand, deep convolutional neural network (DCNN) models have been shown to separate
124 complex patterns into different categories at a human level (LeCun et al., 2015). We apply a
125 transfer learning approach to our classification task in a supervised fashion although separate
126 efforts of unsupervised training also seem promising (Yuan, 2019).
127

128   Specifically, we use a pretrained model (Simonyan & Zisserman, 2015) as a feature extractor
129   and fine-tune it with our training set. The pretrained model is a 16-layer DCNN that is trained
130   on the large-scale ImageNet dataset (Deng et al., 2009). Its weights are fixed. We add three
131   additional layers to the pretrained model, called VGG-16 and train the resulting full model on
132   our training set, the fine-turning step. The output of the full DCNN model is a six-element
133   vector whose elements sum up to 1 and are interpreted as the probability that the model
134   assigns to one of the corresponding types. We assign every scene to the type that has the
135   highest probability and therefore effectively we have a metric to measure how confident the
136   model is for each classification, which provides useful information for users who may apply
137   filters to the data.
138
139   To build the training set, our team together with several expert level volunteers first manually
140   labeled thousands of scenes using the Zooniverse online tool. We retain only those scenes that
141   are unambiguously belonging to a certain type to present the best possible training set, which
142   includes hundreds of samples for each type. We augment the training set by rotating each
143   scene by 90 and 180 degrees and also flipping the open cellular scenes to increase their sample
144   size. The flipping operation is achieved by mirroring the original image across a horizontal axis.
145

146   **3. Results**
147   Here we report results for the training, show the classification at work at a granule level and for
148   two typical low marine low cloud regimes: winter time mid-latitude region downwind of the
149   East Coast of US and Canada and sub-tropical Southeast Pacific region.
150

151   a.   Training performance
152   The training asymptotically converges to a plateau in terms of accuracy pretty quickly, within
153   about 30 epochs (Figure 5). Around epoch 30, the validation accuracy reaches a maximum. The
154   training and validation accuracies are at around 98% and 93%. We save the model configuration
155   with the best validation accuracy. After training, the model is applied to a test set that it has
156   never seen before. The resulting confusion matrix is shown in Figure 6. The confusion matrix
157   summarizes the classification prediction results. For each cloud type, or row, it shows the
158   percentage of correct predictions on the diagonal and percentages of incorrect predictions off
159   the diagonal. The trained model achieves an average precision of about 93% across different
160   types. Open cellular and disorganized cellular convection, are the two morphology types with
161   the lowest accuracy mainly because they had the lowest number of training samples. With
162   further increase in training samples in the future, we are confident that corresponding
163   accuracies can be further improved. The biggest challenge for the model comes from separating
164   disorganized cellular, open cellular, and clustered cumulus types. It is also worth noting that
165   there is inherent uncertainty with the classification since even expert labelers sometimes
166   disagree on the same scenes.
167

168   b.   An example granule
169   An example of a classified MODIS granule is shown in Figure 7. The classification results are
170   overlaid on the visible MODIS image as colored circles whose position represents the center of
171   corresponding 128x128 scene. This is a low cloud dominated granule with a complex mix of

172 different morphology types. The few missing scenes within the viewing zenith angle limits are
173 due to subvisible high clouds overlapping the visible low clouds, which is not rare even for these
174 low cloud dominated regions (Yuan and Oreopoulos, 2013), as well as a couple of scenes with
175 too little low clouds. One can visually confirm that the model performs quite well in picking up
176 morphology types and their transitions corroborating the results in Figure 5.
177
178 c. Test run over the wintertime Northwest Atlantic
179 During the winter, there can be many cold air outbreak events over the Northwest Atlantic
180 region. They create maritime low cloud systems with various mesoscale morphology types. We
181 apply our model to data in winter of 2011. We first filter the raw data to include only marine
182 low cloud scenes using the criteria discussed in section 2. The 128x128 pixel scenes are fed into
183 the trained DCNN model for classification. For each scene, we record its morphology type,
184 geolocation, time and save the 2-D MODIS cloud retrieval parameters such as cloud optical
185 depth, cloud droplet effective radius, and cloud top pressure. In this run, we do not oversample
186 the data and therefore scenes do not overlap with each other.
187
188 Figure 8 shows frequency of occurrence maps for each cloud type along with surface wind
189 vectors. Stratus clouds dominate in the Hudson Bay and Labrador Sea. They also frequently
190 appear over waters around Newfoundland and, to a lesser degree, along the east coast of US
191 and Canada. There is also a local maximum in the western part of the Gulf of Mexico. Closed
192 cellular type dominates the warm water of the Gulf Stream where cold continental air meets
193 the warm water, which induces large flux of moisture and heat from the ocean into the
194 boundary layer and gives rise to formation of low clouds. These low clouds mostly appear as the
195 closed cellular type according to MODIS. The disorganized type only appears in significant
196 quantity in the subtropics away from the coast. Open cellular clouds peak in the area south of
197 the Greenland and in the Labrador Sea and have a local maximum that is centered around
198 60°W and 35°N. Both are downwind of the closed cellular cloud peaks. The clustered and
199 suppressed cumulus clouds mostly occur in the subtropics and tropics.
200
201 d. Results over the Southeast Pacific region
202 We obtained all relevant Aqua MODIS level-1b and level-2 files for the Southeast Pacific region
203 (5°S-45°S, 70°W-125°W) between 2003 and 2018. The total volume of data is about 30 Tb. This
204 region is well known for the semi-permanent stratocumulus clouds.
205
206 Figure 9 shows the 16-year climatology of sea surface temperature (SST), estimated inversion
207 strength (EIS) (Wood and Bretherton, 2006), and frequency of occurrence maps for each
208 morphology type in the Southeast Pacific region. The frequency is normalized by the number of
209 total MODIS scenes, including both low cloud and non-low cloud ones.
210
211 Stratus clouds predominantly occur near coastal upwelling regions in the subtropics as well as
212 in the mid-latitude regions south of 40 degrees. Both features agree with our expectations.
213 Stratus can still occur in other parts of the domain, but with frequencies generally below 10%.
214 Their frequency significantly drops away from the local maxima in the mid-latitudes and along
215 the coast. The local maxima of stratus occurrence frequency coincide spatially with cold SST.

216

217 The closed cellular type occurs most frequently about five hundred kilometers away from the
218 coastlines. The absolute maximum is located around 27°S and 75°W, which is also where EIS
219 peaks. Indeed, the frequency of closed cellular type roughly correlates with the EIS pattern. The
220 frequency of this type drops off from its peak location more gradually compared to that of the
221 stratus. Its frequency is nevertheless below 10% west of 90°W and the direction of the
222 frequency of occurrence gradient is almost east to west. The location of peak frequency for the
223 disorganized type is further away from the coast and occurs around 21°S and 89°W. The
224 frequency map of this type also has an overall correlation with the EIS west of 90°W.

225

226 The frequency map for the open cellular type is the most distinct. Its peak features a bullseye
227 pattern and occurs further downwind of the peak of the disorganized type, with a peak
228 frequency of only about 10%. This type also appears relatively frequently in the mid-latitudes
229 associated with mid-latitude cyclones. Its spatial pattern has no direct correlation with either
230 EIS or SST patterns, possibly implying internal mechanisms that are responsible for their
231 appearances. Both the closed and open cellular locations agree qualitatively with the findings
232 from Wood and Hartmann (2006), although the addition of other cloud types resulted in lower
233 frequencies of these types in our dataset. It is also worth mentioning that the disorganized
234 cellular type has a different geographic occurrence when compared to Wood and Hartmann
235 (2006). This is because under that classification scheme, 'disorganized' includes the bulk of
236 scenes which we classify as suppressed and clustered; the more narrowly-defined disorganized
237 cellular type in our classification is geographically more closely associated with the other
238 cellular cloud types. The clustered cumulus type occurrence appears to have a general
239 anticorrelation with the EIS map. The suppressed cumulus type occurs most frequently in the
240 tropics where the SST is the warmest.

241

242 **4. Discussions and future work**
243 a. Notable new insights
244 Open cellular clouds are less prevalent than previously thought (Atkinson and Zhang, 1996;
245 McCoy et al., 2017; Muhlbauer et al., 2014), especially in subtropical regions. We attribute this
246 to the combination of advanced quantitative observation techniques developed here and the
247 delineation of clustered cumulus and open cellular types. The early studies did not have
248 comprehensive observations to rely on. The more recent results may have included the two
249 types together into the open cellular type, which overestimated the occurrence frequency of
250 the open cellular type in the subtropics. However, given the relatively minor presence of
251 clustered cumulus type in the midlatitudes, the open cellular type may indeed be quite
252 prevalent there, which agrees with previous studies.

253

254 There is a strong spatial correlation between both EIS and SST and the frequency of stratus in
255 two regions analyzed, especially north of 35°N, suggesting a strong control of atmospheric
256 stability and cold SST on this cloud type in higher latitude regions. Their control on other cloud
257 types may not be as tight given the loose spatial correspondence between both EIS and SST and
258 frequency of other cloud types, implying either other large-scale variables are in control or
259 internal cloud processes are more important. We will leave such explorations for future studies.

260
261   b. Expanding the scale of test runs and further analysis
262   We plan to expand the test run to near-global scales for about two years. These runs will
263   include time periods that overlap those of several field campaigns that have rich in-situ and
264   ground and airborne remote sensing data. Together with these datasets, the satellite product
265   will help to advance the understanding of low cloud mesoscale morphology. The global scale
266   will also allow us to examine the general distributions of morphology types and intercompare
267   the characteristics of low cloud morphology in different ocean basins. Further data analysis of
268   the current test run and future runs will target questions related to the variability of low cloud
269   morphology and its driving forces. We plan to release part or all of the test run results to beta
270   testers for feedback and test use from the community.
271
272   c. Collocating with other satellite sensors and meteorology
273   We plan to collocate each classified low cloud scene with data from sensors like CloudSat cloud
274   profiling radar, CALIOP lidar, the Advanced Microwave Scanning Radiometer for EOS (AMSR-E
275   and AMSR-2), and Atmospheric InfraRed Sounder (AIRS) as well as the MERRA-2 reanalysis
276   products. Such collocated set of variables will be useful to the research community for studying
277   the behavior of low cloud morphology under different environmental conditions
278
279   d. Further improvement of the model
280   The current model works pretty well overall, particularly for closed cellular, suppressed
281   cumulus and clustered cumulus types. However, there is room to improve for other types. We
282   target two fronts for improvement: improving the model itself and increasing the quality and
283   quantity of training data. For the former goal, we plan to test different pre-trained models and
284   what features to keep and how to best set up the classifier on top of these extracted feature
285   vectors. For the latter goal, we have developed analysis tools to help us understand the
286   agreement among human experts in the training set. This helps us to target types that need the
287   improvement. We will use the Zooniverse tool to achieve this. Further increase in training data
288   also allows us to better characterize the uncertainty in expert labeling of each category. We are
289   looking for expert level volunteers to join us to increase the training sample size.
290
291   e. Increasing the number of types
292   Some of the mesoscale types can be further divided into subtypes. For example, the frequency
293   of suppressed cumulus type is quite high in the low latitudes and based on the manual labeling
294   they could be further divided into multiple subtypes. We will explore the feasibility of this by
295   assessing resource constraints and the feedback from the community.
296
297
298   **5. Conclusions**
299   We have developed a working deep neural network model to automatically classify cloudy
300   scenes into six mesoscale morphology types. Initial test run results showed promising results
301   for the Southeast Pacific and Northwest Atlantic. Using the tool, we plan to extend the dataset
302   and create a community mesoscale morphology type product for low marine clouds observed

303 by MODIS. We will further develop the product and actively look forward to community
304 involvement such as beta testing, volunteering, and user feedback.
305
306
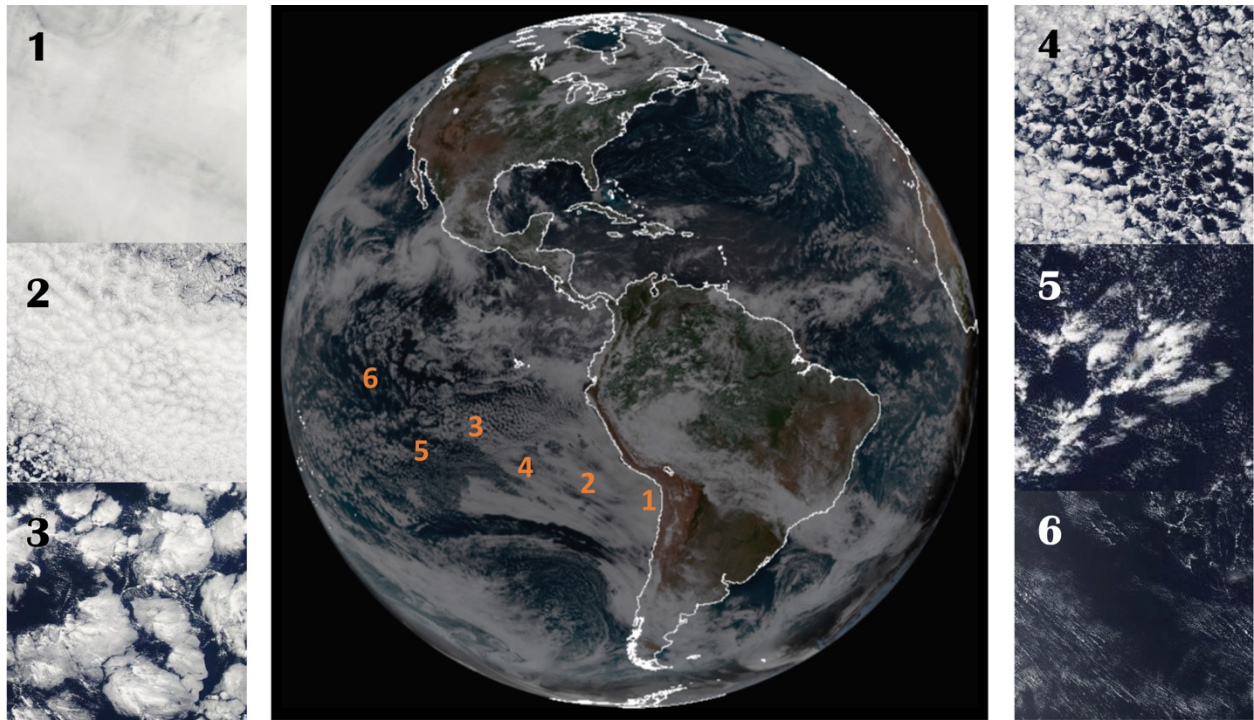
307
308 Figure 1: A full disk image of GOES-16 on Aug 6, 2018 and six scenes of MODIS images at smaller
309 scales representing different morphology types at corresponding locations in the GOES image.
310 Except scene 1, all scenes are from the same day. Scene 1 is from a different day because there
311 was no representative stratus scenes on this day in the Southeast Pacific region.
312
313
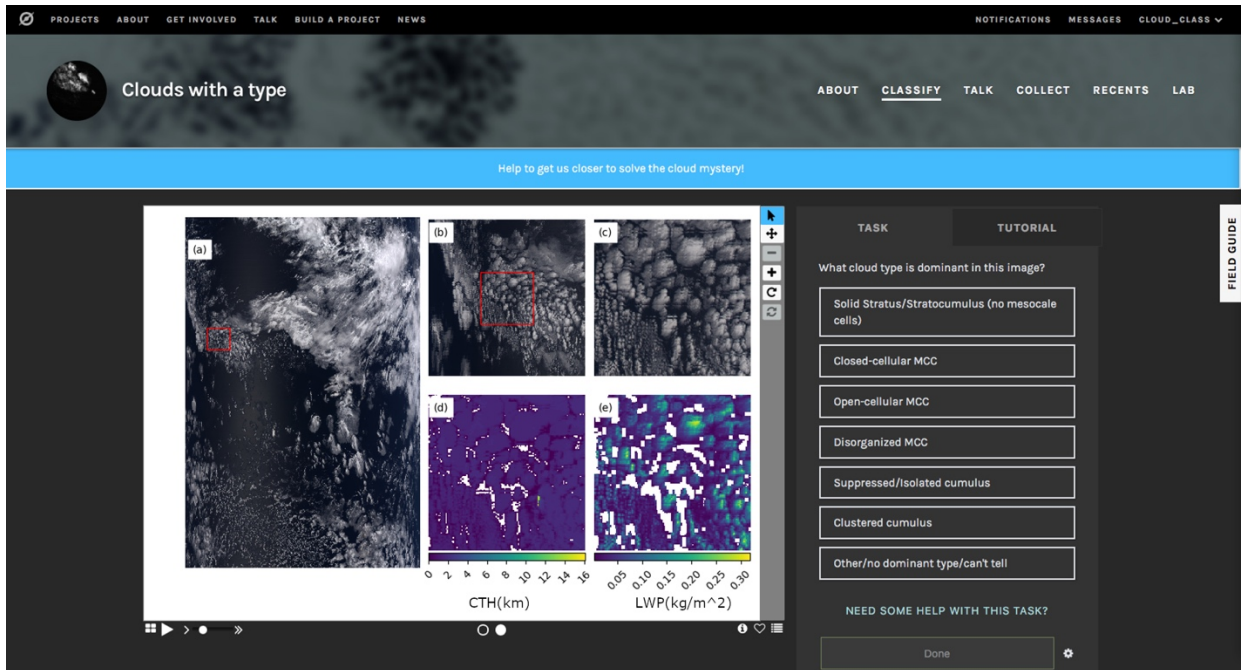
314
315 Figure 2: the Zooniverse interface for manual labelling. The center image is made up of five
316 panels. Panel a shows the full granule (usually 2030x1350 pixels) true color image for large
317 context. Panel b shows a portion of the granule immediately surrounding the scene to be
318 labelled, outlined by the red square. Panel c shows the visible scene image while panels d and e
319 show the cloud top height and LWP fields in the scene to be labelled. The panels to the right of
320 the center image show labelling choices. The tutorial document is available by clicking on the
321 'FIELD GUIDE' tab on the right side. Additional options for scenes with heavily mixed types,
322 scenes with sea ice, or scenes with other issues are found in the 'other' menu. The image is a
323 screenshot of our Zooniverse project.

324
325
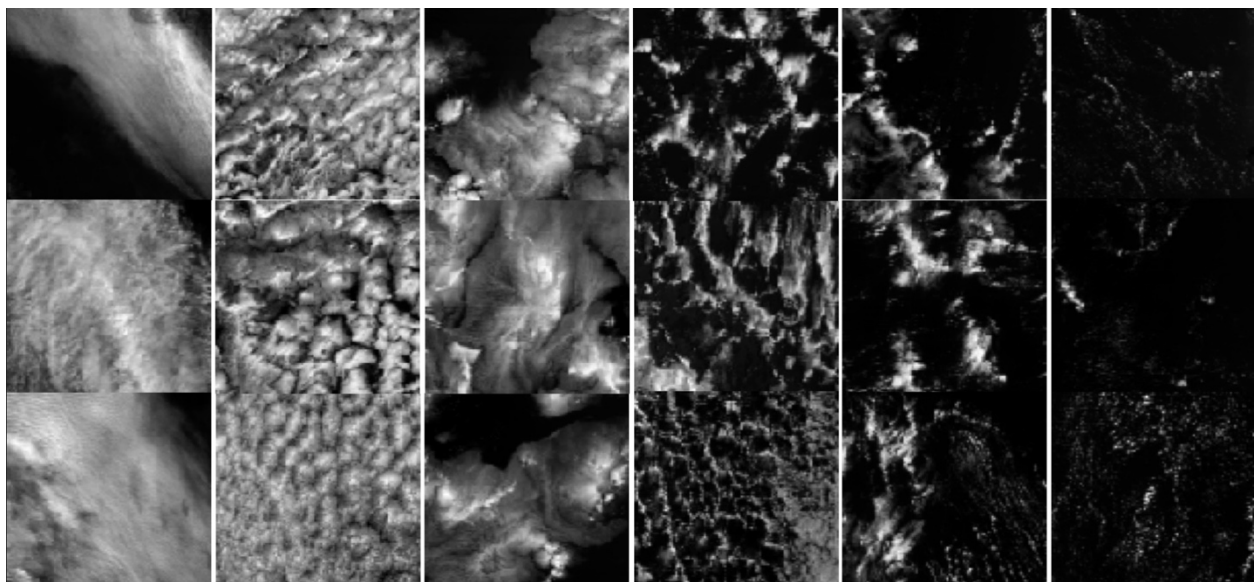
326
327

328 Figure 3: Example scenes of MODIS single channel images for the six different types. From left
329 to right: stratus, closed cellular, disorganized cellular, open cellular, clustered cumulus, and
330 suppressed cumulus types. Images taken by the NASA MODIS.

331
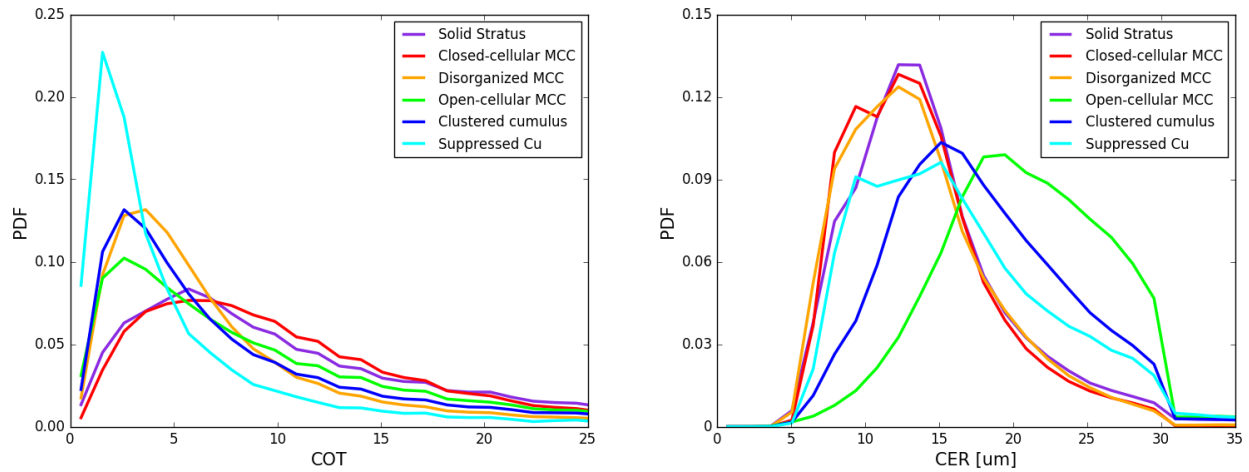
332
333
334 Figure 4: PDFs of cloud optical depth and cloud effective radius for six morphology types.
335 Significant overlaps are observed for PDFs of both variables among different morphology types.

336
337

338

339 Figure 5: Training (upper two panels) and validation (lower ones) accuracy and loss trajectories.
340 By around epoch 30, the validation accuracy peaks while validation loss bottoms out and the
341 training loss and accuracy asymptotically reach their minimum and maximum, respectively,
342 which indicates further training may be overfitting the model.
343
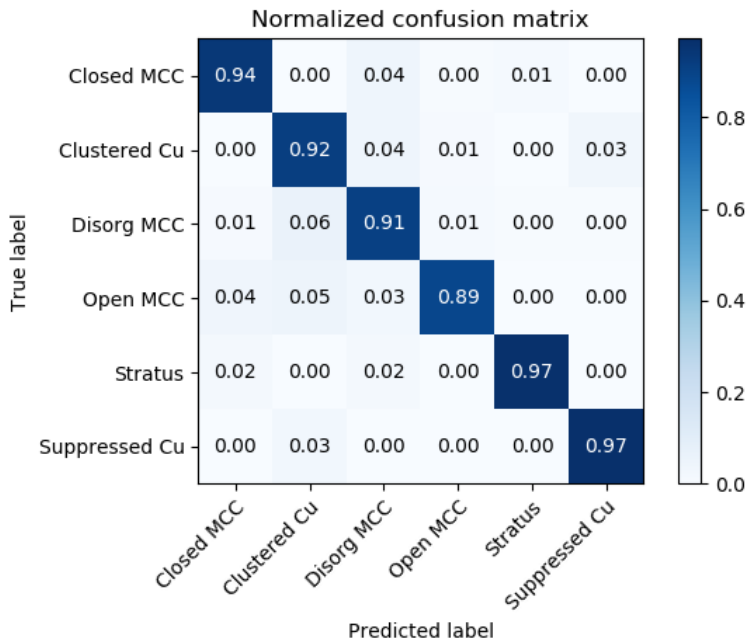
344
345 Figure 6: Confusion matrix of the model predictions on test data.
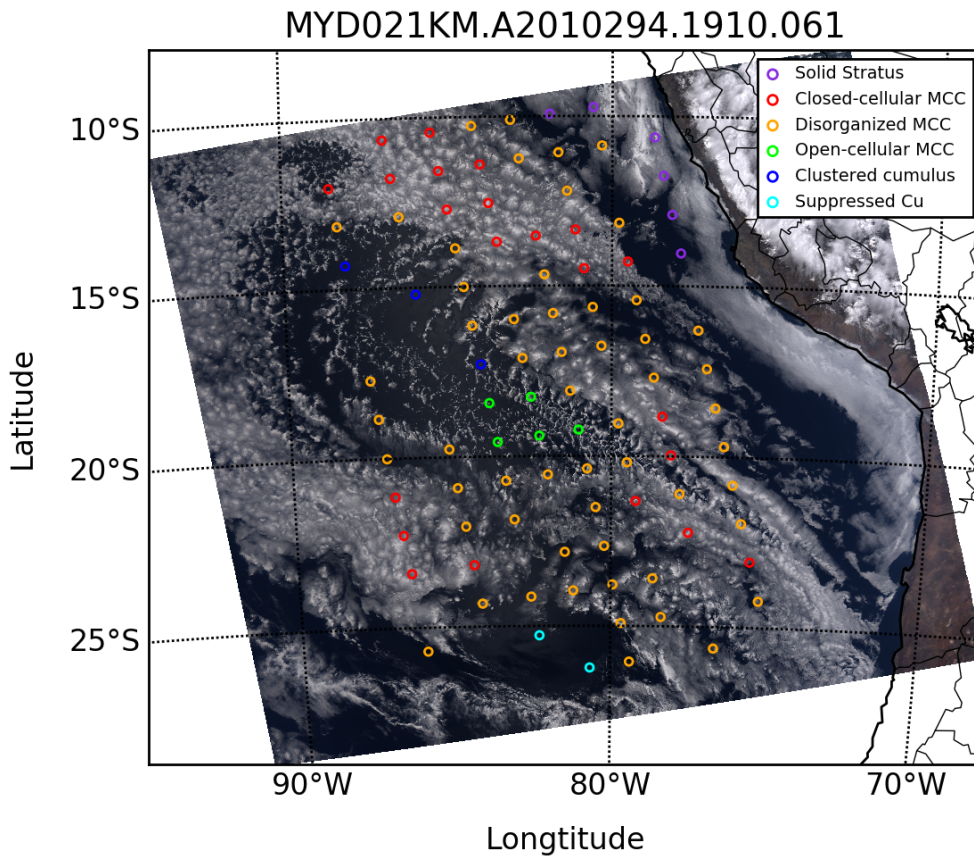
Figure 7: An example granule illustrating the results of the classification algorithm. This is quite
a complex granule with different morphology types mixed together. The left and right margins
are not classified because current algorithm filters out scenes whose sensor viewing zenith
angles are greater than 45 degrees. The image is taken by NASA MODIS.
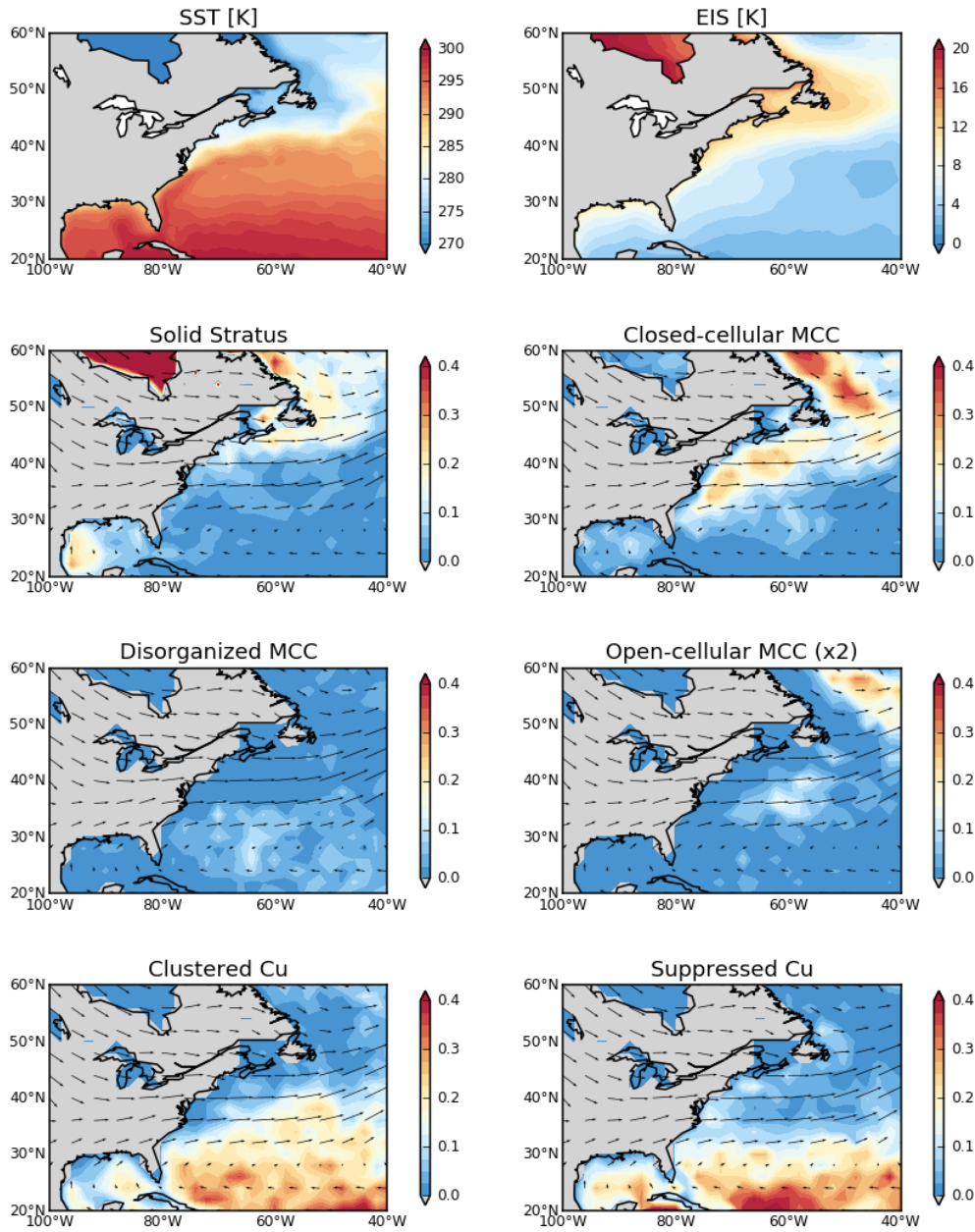
Figure 8: Frequency distributions of six morphology types obtained from the classification algorithm in the Northwest Atlantic region off the east coasts of US and Canada in the winter of 2011. The top two panels show the SST and EIS distributions using MERRA-2. Seasonal mean wind vectors at 850hPa are plotted to illustrate the flow. We double the values for frequency of the open-cellular type to make them numerically comparable with other types.
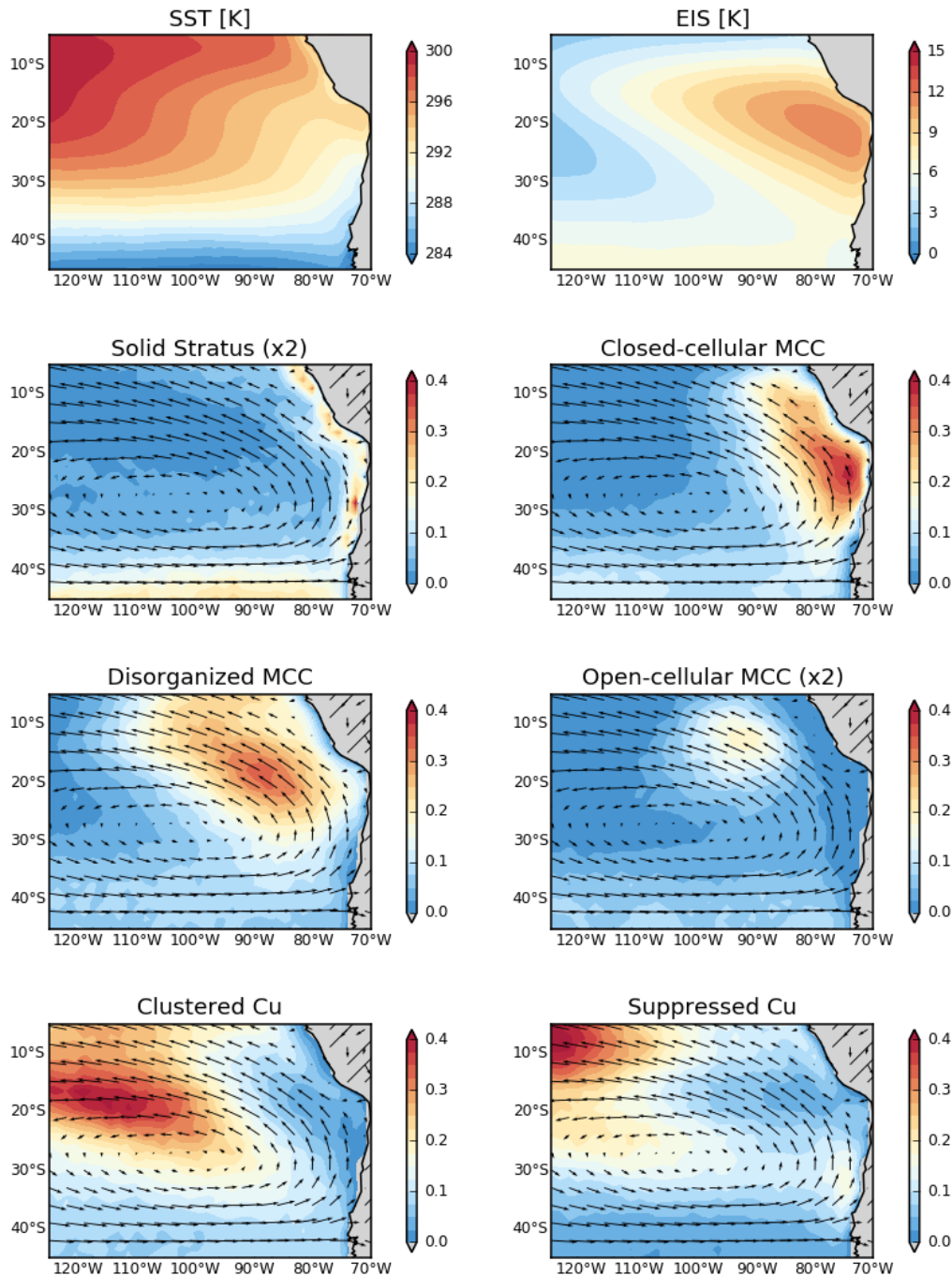
Figure 9: Frequency distributions of various morphology types obtained from the classification algorithm in the subtropical eastern Pacific off the coast of South America for the period 2003-2018. The top two panels show the SST and EIS climatology from MERRA-2 for the same period. Note the doubling of scale on the stratus and open-cellular types.

6. Author Contribution

367 T. Y. implemented the method to train the network model. H. S., J. M., and T.Y. prepared the
368 training data. All co-authors contributed to compiling the training dataset. T. Y. wrote the
369 manuscript with contributions from all co-authors.
370

371 **7. Reference**

372 Agee, E. M., & Dowell, K. E. (1974). Observational Studies of Mesoscale Cellular Convection.

373 *Journal of Applied Meteorology*, *13*(1), 46–53. https://doi.org/10.1175/1520-

374 0450(1974)013<0046:OSOMCC>2.0.CO;2

375 Atkinson, B. W., & Zhang, W. J. (1996). Mesoscale shallow convection in the atmosphere.

376 *Reviews Of Geophysics*, *34*(4), 403–431. https://doi.org/10.1029/96RG02623

377 Deng, J., Dong, W., Socher, R., Li, L.-J., Kai Li, & Li Fei-Fei. (2009). ImageNet: A large-scale

378 hierarchical image database. In *2009 IEEE Conference on Computer Vision and Pattern*

379 *Recognition* (pp. 248–255). https://doi.org/10.1109/CVPR.2009.5206848

380 Gelaro, R., McCarty, W., Suárez, M. J., Todling, R., Molod, A., Takacs, L., et al. (2017). The

381 Modern-Era Retrospective Analysis for Research and Applications, Version 2 (MERRA-2).

382 *Journal of Climate*, *30*(14), 5419–5454. https://doi.org/10.1175/JCLI-D-16-0758.1

383 LeCun, Y., Bengio, Y., & Hinton, G. (2015). Deep learning. *Nature*, *521*(7553), 436–444.

384 https://doi.org/10.1038/nature14539

385 McCoy, I. L., Wood, R., & Fletcher, J. K. (2017). Identifying Meteorological Controls on Open and

386 Closed Mesoscale Cellular Convection Associated with Marine Cold Air Outbreaks.

387 *Journal of Geophysical Research: Atmospheres*, *122*(21), 11,678-11,702.

388 https://doi.org/10.1002/2017JD027031

389   Muhlbauer, A., McCoy, I. L., & Wood, R. (2014). Climatology of stratocumulus cloud

390   morphologies: microphysical properties and radiative effects. *Atmospheric Chemistry*

391   *And Physics*, *14*(13), 6695–6716. https://doi.org/10.5194/acp-14-6695-2014

392   Platnick, S., Meyer, K. G., King, M. D., Wind, G., Amarasinghe, N., Marchant, B., et al. (2017). The

393   MODIS Cloud Optical and Microphysical Products: Collection 6 Updates and Examples

394   From Terra and Aqua. *IEEE Transactions on Geoscience and Remote Sensing*, *55*(1), 502–

395   525. https://doi.org/10.1109/TGRS.2016.2610522

396   Simonyan, K., & Zisserman, A. (2015). Very Deep Convolutional Networks for Large-Scale Image

397   Recognition. *ArXiv:1409.1556 [Cs]*. Retrieved from http://arxiv.org/abs/1409.1556

398   Stevens, B., Vali, G., Comstock, K., Wood, R., van Zanten, M. C., Austin, P. H., et al. (2005).

399   Pockets of open cells and drizzle in marine stratocumulus. *Bulletin Of The American*

400   *Meteorological Society*, *86*(1), 51—-. https://doi.org/10.1175/BAMS-86-1-51

401   Wang, H., & Feingold, G. (2009). Modeling mesoscale cellular structures and drizzle in marine

402   stratocumulus. Part I: Impact of drizzle on the formation and evolution of open cells.

403   *Journal Of The Atmospheric Sciences*, *66*(11), 3237–3256.

404   https://doi.org/10.1175/2009JAS3022.1

405   Wood, R, & Bretherton, C. S. (2006). On the relationship between stratiform low cloud cover

406   and lower-tropospheric stability. *Journal Of Climate*. Retrieved from

407   http://journals.ametsoc.org/doi/pdf/10.1175/JCLI3988.1

408   Wood, Robert. (2012). Stratocumulus Clouds. *Monthly Weather Review*, *140*(8), 2373–2423.

409   https://doi.org/10.1175/MWR-D-11-00121.1

410   Wood, Robert, & Hartmann, D. L. (2006). Spatial variability of liquid water path in marine low

411   cloud: The importance of mesoscale cellular convection. *Journal Of Climate*, *19*(9),

412   1748–1764.

413   Yuan, T. (2019). Understanding Low Cloud Mesoscale Morphology with an Information

414   Maximizing Generative Adversarial Network. https://doi.org/10.31223/osf.io/gvebt

415   Yuan, T., & Oreopoulos, L. (2013). On the global character of overlap between low and high

416   clouds. *Geophysical Research Letters*, *40*(19), 5320–5326.

417   https://doi.org/10.1002/grl.50871

418

419
420
421
422
423
424
425
426
427
428
429
430
431
432
433
434
435
436
437
438
439
440
441
442
443
444

445
446